JOURNAL OF MATERIAL SCIENCE 28 (1993) 1910–1918

The effect of surface-limited microcracks on the effective Young's modulus of ceramics

Part III *Experiments*

Y. KIM, E. D. CASE, S. GAYNOR
Department of Metallugry, Mechanics and Materials Science, Michigan State University, East Lansing, MI 48824-1226, USA

The effect of aligned Vickers indentation cracks upon the Young's modulus of polycrystalline alumina bars was investigated. The measured Young's modulus for indented specimens was compared with the theoretical predictions based on a variety of models, including a model developed by the authors.

1. Introduction

In this study, aligned Vickers indentation cracks in polycrystalline alumina bars served as a model population of surface-limited microcracks. The ability to control and measure the number, location and size of the indentation-induced surface cracks facilitates the comparison between theory and experiment. Changes in the Young's modulus were measured as a function of the number and size of Vickers indentation cracks placed on the specimen surfaces.

Two types of composite layer model for surface-limited microcracking damage were considered: (i) a dynamic modulus model and (ii) a rule-of-mixtures (ROM) model [1, 2]. In both types of models, the modulus of the crack-damaged layer(s) is reduced according to the number, size and geometry of indentation cracks present on the specimen surface [1–5]. The dynamic modulus model for half-ellipse cracks modified to account for the indentation-induced plastic zone models the experimental results well.

2. Experimental procedure

2.1. Material preparation and characterization

Polycrystalline alumina (AD-96, Coors Ceramics Co.) billets were cut into prismatic bars using a low-speed diamond saw (Buehler Isomet). The specimens were polished with 3 μm diamond paste to a mirror finish before annealing at 850 °C in air for 12 h. The purpose of the anneal was to relieve the residual stresses which may have been generated during the cutting and polishing of the specimens. The mass densities of the specimens were determined from measured mass and specimen dimensions (Table I). The mean grain size of 6 to 7 μm was determined by the linear intercept technique on SEM micrographs of fractured surfaces.

2.2. Microindentation and fractography

Aligned microcracks were generated on the long transverse surfaces of the alumina bars (Fig. 1) by Vickers microindentation (Digital Semimacrohardness Tester, Buehler Ltd). Loads of 49, 98 and 196 N were used with a loading speed of 70 $\mu m\,s^{-1}$ and a loading time of 10 s. The indentation crack field for each specimen consisted of two subgroups of cracks, with one subgroup oriented longitudinally and the other subgroup oriented transversely on the specimen surface (Fig. 2).

For each of the three indentation loads, pairs of nominally identical specimens were indented. One specimen of the pair was indented on a single long transverse surface only and the other specimen of the pair was indented on both of the long transverse surfaces. Specimens indented on both long transverse surfaces were indented alternatively on the top and bottom surfaces. The spatial arrangement of indentation cracks is illustrated in Fig. 2. The average spacing between the indentations was 2.2 mm.

Radial crack lengths were measured using an optical microscope mounted on the indenter, which utilized a digital readout accurate to within $\pm$ 0.1 μm.

To directly observe the geometry and depth of the indentation-induced cracks without causing the cracks to extend under and an applied load, this study employed a fractographic technique used by Kirchner and Issacson [6, 7] and Symonds *et al.* [7]. In those studies, specimens abraded on a single surface were fractured in four-point bend. The specimens were oriented in the bend test fixture so that the undamaged surface of the specimen was the tensile surface, and the compression surface was the abrasion-damaged face. The macrocrack which caused catastrophic failure thus grew from the tensile surface, driven by the four-point loading stresses. The macrocrack thus intersected the damaged surface (compression surface) only slightly before the final instant of specimen failure. Thus a set of relatively unperturbed surface microcracks were revealed by intersection with the plane of the advancing macrocrack [6–8]. The success of this technique, of course, depends on

0022–2461

TABLE I Dimensions and densities of prismatic bar-shaped alumina specimens

Indentation load[a]	Thickness (cm)	Width (cm)	Length (cm)	Density ($g\,cm^{-3}$)
49 N (S)	0.1000	1.20	6.390	3.758
49 N (B)	0.1010	0.612	6.870	3.680
98 N (S)	0.1014	1.20	6.943	3.734
98 N (B)	0.1000	1.20	7.070	3.757
196 N (S)	0.1005	1.20	6.970	3.755
196 N (B)	0.1000	1.20	6.850	3.742

[a] B = Indented both long transverse surfaces, S = indented only on a single surface.

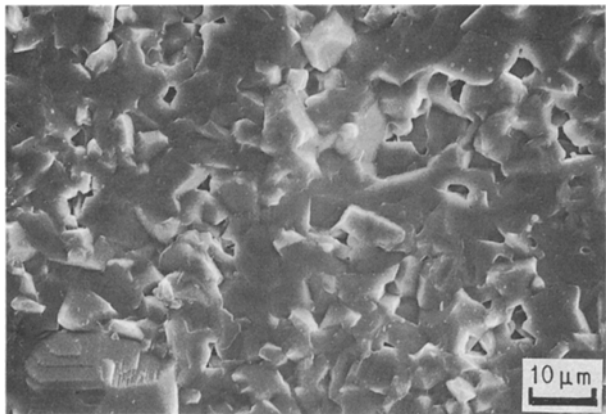

Figure 1 SEM micrograph of fracture surface of polycrystalline alumina specimen (bar represents a length of 10 μm).

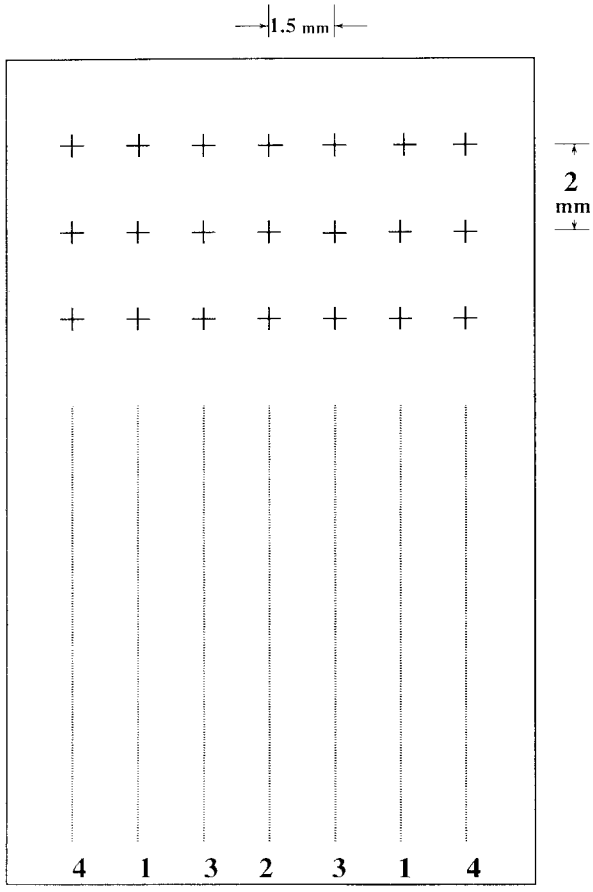

Figure 2 Spatial arrangement of indentation cracks for specimen indented on a single surface at a load of 98 N. The spatial arrangement of indentation cracks was similar for other specimens.

the surface crack number density on the specimen's compression face. If the surface cracks are too sparse, then the advancing macrocrack may not intersect one of the microcracks of interest.

When the indentation measurements and the elastic modulus measurements were complete for a given specimen (section 2.3), indentation-damaged specimens in this study were oriented in a four-point bend fixture with an indented surface on the compression side of the bend bar. The four-point bend fixture had an upper span of 20 mm, a lower span of 40 mm and a roller diameter of 3.1 mm. Specimens indented at each of the three different loads (49, 98 and 196 N) were then fractured in four-point bend, which allowed a macrocrack from the bar's tensile surface to propagate down and intercept an indented surface. The geometry of indentation cracks (as revealed on the fracture surface of the bend bars) was then studied via optical and scanning electron microscopy.

In addition to serving as a model array of surface cracks, the Vickers microindentations were also used to determine the hardness and fracture toughness of the specimens [9–11].

2.3. Elastic modulus measurements

The sonic resonance technique and apparatus used for the modulus measurements are described in detail elsewhere [12–20]. The Young's modulus and Poisson's ratio of the undamaged alumina specimens were measured after annealing and prior to indentation [12–15]. Also modulus measurements were made immediately after finishing a preselected number of indentations at each load. For example, for the specimen indented on both long transverse surfaces at 98 N load, the elastic modulus was measured prior to indentation and was then remeasured after 46, 92, 184, 368, 460 and 552 cumulative indentations.

3. Results and discussion

3.1. Measurements on undamaged specimens

Room-temperature values of Young's modulus. Poisson's ratio, fracture toughness and hardness were measured in order to (i) establish the "zero damage" values for the elastic moduli and (ii) provide a check of consistency on the physical property measurements (modulus, fracture toughness and hardness) with the literature.

For the undamaged polycrystalline alumina specimens, the measured Young's modulus was approxim-

ately 320–340 GPa, with a shear modulus of about 138 to 132 GPa and a Poissons's ratio between 0.20 and 0.22. The observed range of undamaged elastic modulus values is consistent with well-known modulus versus porosity relations (see Appendix and Table I).

The hardness and toughness of the alumina specimens determined by indentation were 12.9 GPa and 3.1 MPa $m^{1/2}$, respectively. The fracture toughness and hardness measured for alumina specimens in this study agree reasonably well with the toughness values of 2.9 and 4.6 MPa $m^{1/2}$ reported by Marshall (polycrystalline alumina, DCB method, Table I in Antis *et al.* [11]), toughness values of 2.5–5 MPa $m^{1/2}$ reported by Becher *et al.* [21] and the toughness value of 2.1 MPa $m^{1/2}$ reported by Evans and Charles [9] (sapphire, double torsion method). Polycrystalline alumina hardness values between 13.1 and 20.1 GPa were measured by Lawn and Marshall [10], while Evans and Charles [9] obtained a hardness of 23 GPa for single-crystal alumina (sapphire). Thus the Young's modulus, shear modulus and Poisson's ratio of the as-received specimens agree well with the literature values, while the hardness and toughness values of the as-received specimens are in reasonable agreement with the range of values reported in the literature. Therefore, the measured mechanical properties of the as-received specimens are certainly consistent with "typical" polycrystalline specimens characterized in the literature.

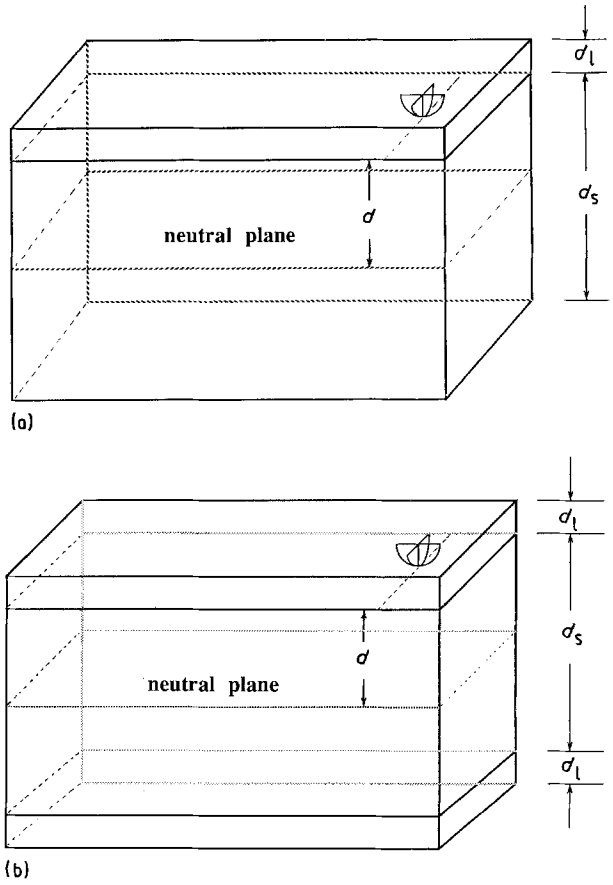

Figure 3 Schematic diagrams of (a) two and (b) three-layer composite models.

3.2. Characterization of indentation cracks

A composite layer damage model developed by two of the authors [1, 2] was used to evaluate the indentation data. Initially, the microcrack-free polycrystalline specimen is characterized by a single, uniform elastic modulus. As indentation damage is introduced into the specimen surface, the surface-damaged regions are modelled as layers of reduced modulus that are "perfectly" bonded to an undamaged substrate (Fig. 3). Specimens indented on a single long transverse surface were thus modelled as a two-layer composite composed of an indentation-damaged layer perfectly bonded to an underlying undamaged layer. Specimens indented on the two long transverse surfaces were modelled as a three-layer composite, with an undamaged middle layer sandwiched between indented top and bottom layers [1, 2] (Fig. 3).

In this study, the microcrack number density was obtained directly from the number of indentations and specimen dimensions. The surface trace of the indentation cracks was measured by optical microscopy directly from the radial crack length. From the total of 1546 indentation cracks generated in this study, the mean radial crack length was computed on the basis of optical measurements from 298 of the indents, or about one-fifth of the total number of indents generated in the study (Table II). The mean radial crack length, determined optically using the Vickers microindenter, agreed to within approximately 15 to 20% with the fractographic measurements of the major axis length of the indent cracks (Fig. 4).

TABLE II Mean radial crack lengths as a function of indent load, as measured optically for the indicated number of indentation sites

Load (N)	Radial crack length (mm)	Number of radial crack lengths measured	Total number of indents per specimen[a]
49	0.2276 ± 0.0203	128	280 (S), 260 (B)
98	0.3701 ± 0.0351	132	238 (S), 552 (B)
196	0.6448 ± 0.0319	38	150 (S), 66 (B)

[a] S indicates that only a single long transverse face of the specimen was indented, while B indicates that both long transverse faces of the specimen were indented.

The shape and depth of the indentation cracks were determined fractographically, since these parameters were not accessible directly from the surface of the indented alumina bars. For each of the three indentation loads used in this study, the indentation-induced cracks were elliptical (Fig. 4) with the major axis oriented along the specimen surface and the minor axis perpendicular to the specimen surface.* The crack "depth" thus corresponds to the minor axis of the indentation cracks. Five crack depth measurements were made for the indentation loads of 49 and 98 N,

* The indentation cracks were of the "halfpenny" type (Fig. 4) rather than the Palmqvist type [2]. However, rather than having the idealized semi-circular shape, the indentation cracks were somewhat elliptical.

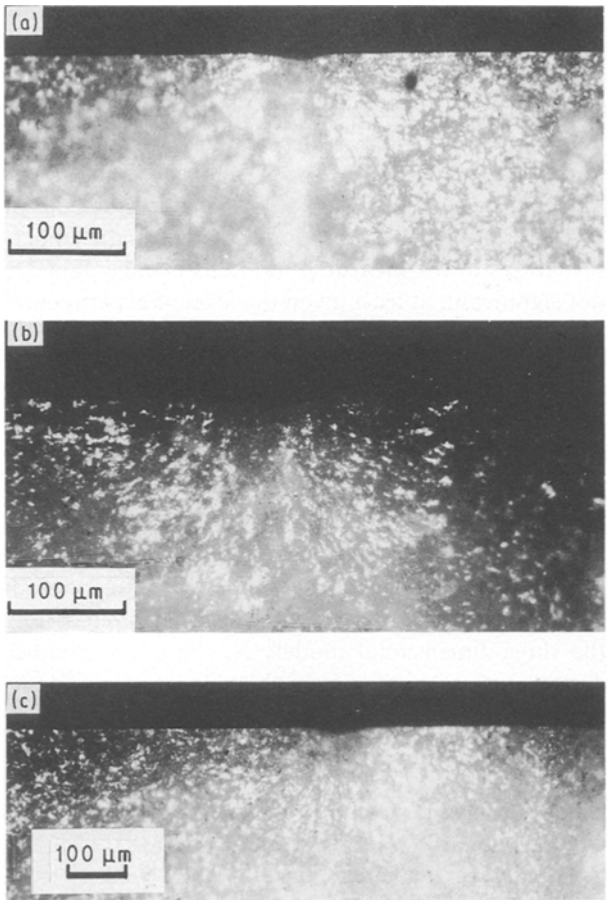

Figure 4 Micrographs of compression-side fracture surface for specimens fractured in four-point bend. The micrographs show the shape and size of the median crack for (a) 49 N, (b) 98 N and (c) 196 N load indentations.

while three crack depth measurements were made for the indentation load of 196 N.

The optically determined mean radial crack lengths were determined for up to 100 or more indentations at a given load (Table II), while the fractographic measurements of crack depth were determined for relatively few cracks. Thus, the statistics of the radial crack lengths were very much better than the statistics for the crack depth measurements.

In order to take advantage of the good radial crack length statistics, an "effective crack depth" was determined in the following way. The ratio of crack depth to radial crack length was assumed to be constant at each load. The "effective crack depth" was computed by multiplying the mean radial crack length (Table II) by the radial crack length/crack depth ratio measured from the micrographs. Effective depths were calculated to be 0.100, 0.144 and 0.239 mm for the 49, 96 and 196 N loads, respectively, according to the procedure described above. For each of the three loads, the measured mean crack depth and the computed effective crack depth agreed to within 17.7% (Table III).

TABLE III Indentation crack depth as a function of indent load, as measured from micrographs of fracture surface

Load (N)	Crack depth (mm)	Ratio of crack depth to radial crack length	Effective crack depth (mm)
49	0.110 ± 0.010	0.44	0.100
98	0.175 ± 0.023	0.39	0.144
196	0.252 ± 0.025	0.37	0.240

3.3. Modulus decrement as a function of Vickers indentation damage

In this study, the Young's moduli were determined using the fundamental flexural resonance frequencies of prismatic bar-shaped specimens, thus the measured moduli represent the in-plane modulus along the length direction of the specimen [23]. Therefore, we assume that only the cracks that are aligned normal to the specimen length contribute to the Young's modulus change.

The indentation-induced microcrack damage was monitored by changes in the Young's modulus. As indentations were added to the specimen, the Young's modulus decreased from the undamaged Young's modulus value E_s to a modulus value of E for a number density N of indentation cracks. To highlight the changes in modulus resulting from the indentation crack field, the normalized Young's modulus change $(E_s - E)/E_s$ is plotted as a function of N (Fig. 5). The changes in Young's modulus as a function of the indentation crack number density were thus compared with the ROM and dynamic modulus models presented by two of the authors [1, 2].

In agreement with the predictions of both the ROM and the dynamic modulus models of specimens with surface-limited microcrack damage [1, 2], the normalized Young's modulus change, $(E_s - E)/E_s$, increased linearly as the number density of indentations increased (Table IV and Fig. 5). The slopes presented in Table IV were obtained by least-squares fitting of the experimental data to an equation of the form

$$(E_s - E)/E_s = SN \quad (1)$$

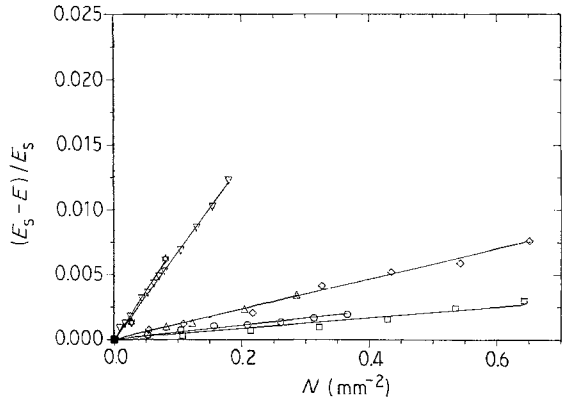

Figure 5 Experimental results for $(E_s - E)/E_s$ versus N (mm^{-2}), where $(E_s - E)/E_s$ is the normalized value of the modulus change due to a surface crack number density N of microcracks. Indented on both surfaces: load (□) 49 N, (◇) 98 N, (☆) 196 N. Indented on single surface: load (○) 49 N, (△) 98 N, (▽) 196 N.

TABLE IV Experimentally determined slope S of $(E_s - E)/E_s$ versus N (mm^{-2}) data, where $(E_s - E)/E_s$ is the normalized value of the modulus change due to a surface crack number density N of microcracks in polycrystalline alumina specimens

Load (N)	Slope, single surface indented	Slope, both surfaces indented
49	$0.539 \times 10^{-2} \pm 0.16 \times 10^{-3}$	$0.475 \times 10^{-2} \pm 0.42 \times 10^{-3}$
98	$1.162 \times 10^{-2} \pm 0.27 \times 10^{-3}$	$1.159 \times 10^{-2} \pm 0.27 \times 10^{-3}$
196	$6.749 \times 10^{-2} \pm 0.49 \times 10^{-3}$	$7.422 \times 10^{-2} \pm 0.61 \times 10^{-3}$

where S is the slope of the $(E_s - E)/E_s$ versus N data. In terms of the ROM and dynamic modulus models, S is equivalent to the product of the crack alignment function f and the crack geometry parameter G [1, 2]. The uncertainties in the experimental slope values (Table IV) were calculated from a commercial linear regression and plotting package (PLOTIT, Scientific Programming Enterprises, Haslett, Michigan). The correlation coefficient for the fit of the data to Equation 1 was greater than 0.993 for each of the six specimens, except for the specimen indented on both long transverse surfaces at a 49 N load, where the correlation coefficient was 0.989.

For a given load, the $(E_s - E)/E_s$ versus N slopes for specimens indented on a single long transverse face and those specimens indented on both long transverse faces agree to within about one standard deviation (Table IV). This similarity between the experimental slopes has important implications for the possible effects of compressive stress on the data. Residual stress fields are known to accompany Vickers indentation [24, 25]. As the number of indentations increases, a developing layer of compressive stress from the indentation crack field might perturb the modulus measurements. While compressive stresses on a single specimen face might slightly perturb the measured modulus, equivalent compressive stresses on two opposing long transverse faces of the specimen should have a zero net effect [26] on the modulus measured by the sonic resonance technique. Compressive stresses thus might slightly perturb the modulus measured for specimens indented on a single specimen face, but such perturbations should be absent for specimens indented on two long transverse faces. The equivalence of the $(E_s - E)/E_s$ versus N slopes for specimens indented on a single face and specimens indented on two faces implies that compressive-stress-induced perturbations of the measured modulus-change data are not significant, at least given the level of experimental uncertainty involved in this study (Table IV).

3.4. Comparison of modulus decrement data with predictions of dynamic modulus and ROM models

The comparison of the theoretical predictions (Part I [1] and Part II [2]) with the experimental results will be presented here in terms of the two categories of three-dimensional and two-dimensional models. For the three-dimensional models N, the crack number density, was calculated from the volume of the "damaged layer" and the number of indents in a given surface, such that N = number of indentations/(depth of microcracked layer × specimen width × specimen length). For the two-dimensional models (see especially Appendix A and Appendix B in Part II [2]), N_a, the area crack number density, was calculated from the relation N = number of indentations/(specimen width × specimen length). For both the three-dimensional and two-dimensional cases, dynamic modulus and ROM models were considered [1, 2]. While the development in Parts I and II was primarily in terms of the three-dimensional damage layer assumption, the two-dimensional case will be considered here for completeness.

For the three-dimensional damage layer case, Fig. 6a (dynamic modulus model) and Fig. 6b (ROM model) compare experimental values of $(E_s - E)/E_s$ versus N (mm^{-3}) with the theoretical predictions from each of six model crack geometries [2] for the particular case of indentation cracks generated at a load of 196 N. Table V (dynamic modulus model) and Table

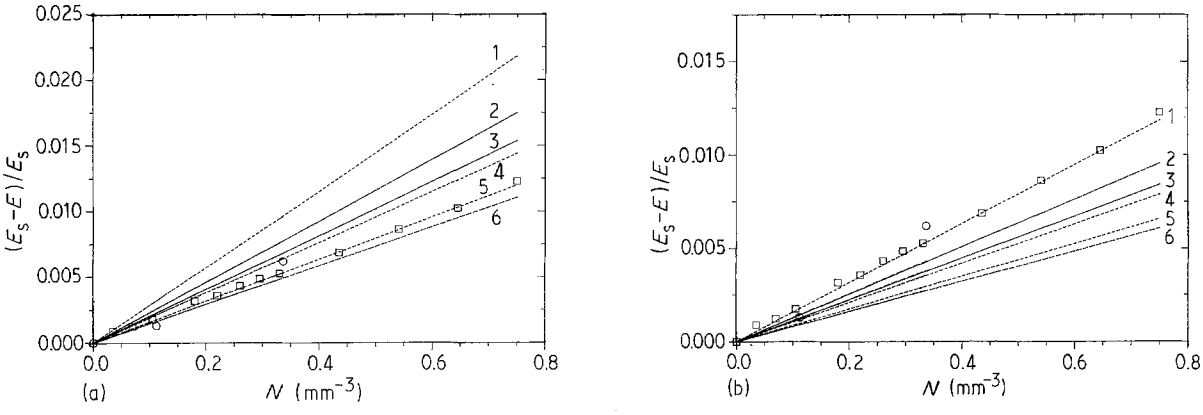

Figure 6 Comparison of experimental values of $(E_s - E)/E_s$ versus N (mm^{-3}), where N is the number density of cracks in the layer, with theory predictions from each of six different crack geometries for 196 N indentations: (○) both surfaces indented, (□) single surface indented. (a) Dynamic beam vibration theory: (1) slit, (2) half-ellipse, (3) modified slit with elliptical indentation bottom, (4) modified slit, (5) modified half-ellipse with elliptical indent bottom, (6) modified half-ellipse. (b) Rule of mixtures: (1) slit, (2) half-ellipse, (3) modified slit with elliptical indentation bottom, (4) modified slit, (5) modified half-ellipse with elliptical indent bottom, (6) modified half-ellipse.

VI (ROM model) compare the numerical values of the experimental $(E_s - E)/E_s$ versus N (mm^{-3}) slopes with the theoretical slope values [1, 2] for each specimen at each of the three load values.

For the three-dimensional dynamic modulus model (Table V), the best correlation between experimental data and theory was obtained for modified half-ellipse cracks and modified half-ellipse cracks with elliptical indent bottom, where "modified" refers to modifications in the crack area and crack perimeter expressions to account for the geometry of the indentation crack (Table II in Part II [2]). For the ROM model (Table VI) the best correlation between experimental data and theory was obtained for half-ellipse cracks for 98 N indentations and three-dimensional slit cracks for 196 N indentations (Table II in Part II [2]).

TABLE V Comparison of experimental values of $(E_s - E)/E_s$ versus N (mm^{-3}) slopes with the dynamic modulus model, assuming various crack geometries [1, 2]; N (mm^{-3}) was calculated from the microcracked layer volume as defined in section 3.3

	49 N indented	98 N indented	196 N indented
Experiment			
Both[a]	0.459×10^{-3}	1.659×10^{-3}	1.773×10^{-2}
Single[a]	0.540×10^{-3}	1.673×10^{-3}	1.613×10^{-2}
Modified slit			
Both	0.669×10^{-3}	2.595×10^{-3}	1.906×10^{-2}
Single	0.679×10^{-3}	2.579×10^{-3}	1.914×10^{-2}
Modified half-ellipse			
Both	0.500×10^{-3}	1.941×10^{-3}	1.465×10^{-2}
Single	0.507×10^{-3}	1.929×10^{-3}	1.470×10^{-2}
Half-ellipse			
Both	0.927×10^{-3}	3.509×10^{-3}	2.304×10^{-2}
Single	0.941×10^{-3}	3.489×10^{-3}	2.321×10^{-2}
Slit			
Both	1.147×10^{-3}	4.333×10^{-3}	2.855×10^{-2}
Single	1.159×10^{-3}	4.318×10^{-3}	2.893×10^{-2}
Modified slit, elliptical indent bottom			
Both	0.678×10^{-3}	2.796×10^{-3}	2.031×10^{-2}
Single	0.686×10^{-3}	2.781×10^{-3}	2.042×10^{-2}
Modified half-ellipse, elliptical indent bottom			
Both	0.507×10^{-3}	2.135×10^{-3}	1.590×10^{-2}
Single	0.513×10^{-3}	2.120×10^{-3}	1.594×10^{-2}

[a] "Both" indicates specimens that were indented on both long transverse surfaces. "Single" indicates specimens that were indented on a single transverse surface.

TABLE VI Comparison of the experimental values of $(E_s - E)/E_s$ versus N (mm^{-3}) slopes with those of theoretical prediction (ROM) assuming various crack geometries; N (mm^{-3}) was calculated from the microcracked layer volume as defined in section 3.3

	49 N indented	98 N indented	196 N indented
Experiment			
Both[a]	0.459×10^{-3}	1.659×10^{-3}	1.773×10^{-2}
Single[a]	0.540×10^{-3}	1.673×10^{-3}	1.613×10^{-2}
Modified slit			
Both	0.282×10^{-3}	1.169×10^{-3}	1.060×10^{-2}
Single	0.284×10^{-3}	1.153×10^{-3}	1.052×10^{-2}
Modified half-ellipse			
Both	0.209×10^{-3}	0.874×10^{-3}	0.815×10^{-2}
Single	0.212×10^{-3}	0.861×10^{-3}	0.810×10^{-2}
Half-ellipse			
Both	0.387×10^{-3}	1.580×10^{-3}	1.283×10^{-2}
Single	0.393×10^{-3}	1.559×10^{-3}	1.272×10^{-2}
Slit			
Both	0.479×10^{-3}	1.952×10^{-3}	1.590×10^{-2}
Single	0.484×10^{-3}	1.926×10^{-3}	1.581×10^{-2}
Modified slit, elliptical indent bottom			
Both	0.283×10^{-3}	1.259×10^{-3}	1.131×10^{-2}
Single	0.287×10^{-3}	1.241×10^{-3}	1.121×10^{-2}
Modified half-ellipse, elliptical indent bottom			
Both	0.212×10^{-3}	0.962×10^{-3}	0.884×10^{-2}
Single	0.215×10^{-3}	0.948×10^{-3}	0.877×10^{-2}

[a] See footnote to Table V.

Since the modulus measurement technique employed in this study was a dynamic technique (sonic resonance, section 2.3) it is to be expected that the dynamic modulus models would generally fit the data better than the ROM models.

For the two-dimensional damage layer case, Fig. 7a (dynamic modulus model) and Fig. 7b (ROM model) compare experimental values of $(E_s - E)/E_s$ versus N (mm^{-2}) with the theoretical predictions from each of the six model crack geometries [2] for the particular case of indentation cracks generated at a load of 196 N. Table VII (dynamic modulus model) and Table VIII (ROM model) compare the numerical values of the experimental $(E_s - E)/E_s$ versus N (mm^{-2}) slopes with the theoretical slope values [1, 2] for each specimen at each of the three load values. For the dynamic modulus model, the agreement between the experimental data and theory [2] was not good for any of the model crack geometries considered (Table VII). For the ROM model (Table VIII) the best agreement between the experimental data and the theory was obtained for "modified" two-dimensional slit cracks (Table VIII).

Fig. 8a–c show the agreement between the experimental data and the modified half-ellipse, dynamic vibration theory (Fig. 8a), the modified half-ellipse with elliptical indent bottom (Fig. 8b), and the modified two-dimensional slit model, rule of mixtures (Fig. 8c). Fig. 8a–c represent the best agreement between theory and experiment for the various models considered in this study. Especially in Fig. 8a and b, the agreement of experiment and theory is relatively good. From the experimental observations of indentation-induced cracks discussed in this study, we feel that the modified half-ellipse model in fact most closely approximates the actual crack geometry. However, no direct experimental measurements were made to determine the relative geometry (semi-circular versus semi-elliptical) of the plastically deformed zone formed by the indentation.

4. Summary and conclusions

Polycrystalline alumina specimens with arrays of Vickers indentation-induced microcracks were used to evaluate models for surface-limited crack damage in a brittle material [1, 2]. For the indentation-induced cracks, the measured fractional Young's modulus changes, $(E_s - E)/E_s$, increased linearly with increasing microcrack number density N, in accordance with the theoretical predictions (Equation 1 and Parts I and II [1, 2]). The observed crack-induced modulus

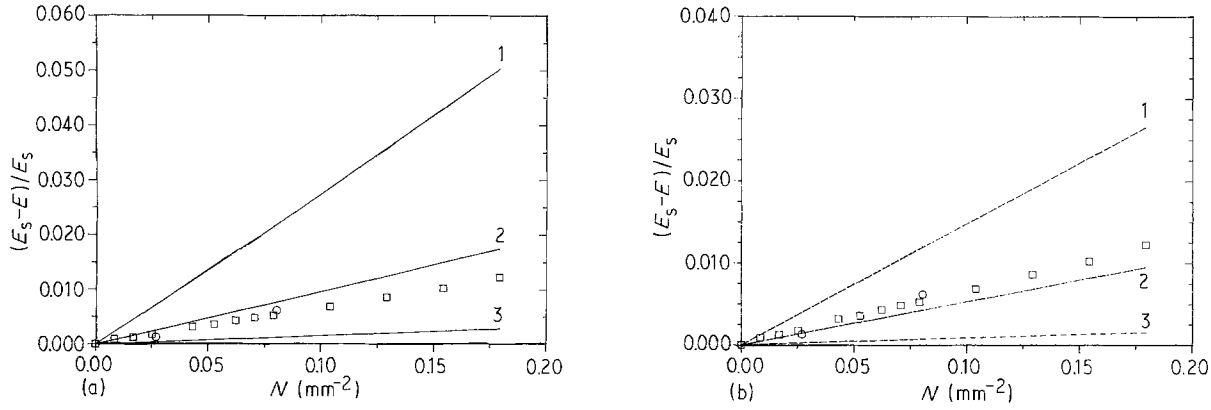

Figure 7 Comparison of experimental values of $(E_s - E)/E_s$ versus N (mm^{-2}), the number density of surface cracks, with theory predictions from each of three different crack geometries for 196 N indentations: (○) both surfaces indented, (□) single surface indented. (a) Dynamic beam vibration theory: (1) 2D slit, (2) modified 2D slit, (3) Palmqvist. (b) Rule of Mixtures: (1) 2D slit, (2) modified 2D slit, (3) Palmqvist.

TABLE VII Comparison of the experimental values of $(E_s - E)/E_s$ versus N (mm^{-2}) slopes with the dynamic modulus model, assuming various crack geometries [1, 2]; N (mm^{-2}) is the surface number density of cracks

	49 N indented	98 N indented	196 N indented
Experiment			
Both[a]	0.475×10^{-2}	1.159×10^{-2}	7.422×10^{-2}
Single[a]	0.539×10^{-2}	1.162×10^{-2}	6.749×10^{-2}
2D slit			
Both	2.020×10^{-2}	6.589×10^{-2}	0.2688
Single	2.055×10^{-2}	6.611×10^{-2}	0.2770
Modified 2D slit			
Both	0.843×10^{-2}	2.437×10^{-2}	9.640×10^{-2}
Single	0.855×10^{-2}	2.423×10^{-2}	9.713×10^{-2}
Palmqvist			
Both	0.859×10^{-3}	3.209×10^{-3}	1.595×10^{-2}
Single	0.869×10^{-3}	3.186×10^{-3}	1.588×10^{-2}

[a] See footnote to Table V.

TABLE VIII Comparison of the experimental values of $(E_s - E)/E_s$ versus N (mm^{-2}) slopes with those of theoretical prediction (ROM) assuming various crack geometries; N (mm^{-2}) is the surface number density of cracks

	49 N indented	98 N indented	196 N indented
Experiment			
Both[a]	0.475×10^{-2}	1.159×10^{-2}	7.422×10^{-2}
Single[a]	0.539×10^{-2}	1.162×10^{-2}	6.749×10^{-2}
2D slit			
Both	0.844×10^{-2}	2.967×10^{-2}	0.1493
Single	0.856×10^{-2}	2.926×10^{-2}	0.1482
Modified 2D slit			
Both	0.352×10^{-2}	1.097×10^{-2}	5.369×10^{-2}
Single	0.357×10^{-2}	1.082×10^{-2}	5.324×10^{-2}
Palmqvist			
Both	0.358×10^{-3}	1.444×10^{-3}	8.855×10^{-3}
Single	0.368×10^{-3}	1.428×10^{-3}	8.821×10^{-3}

[a] See footnote to Table V.

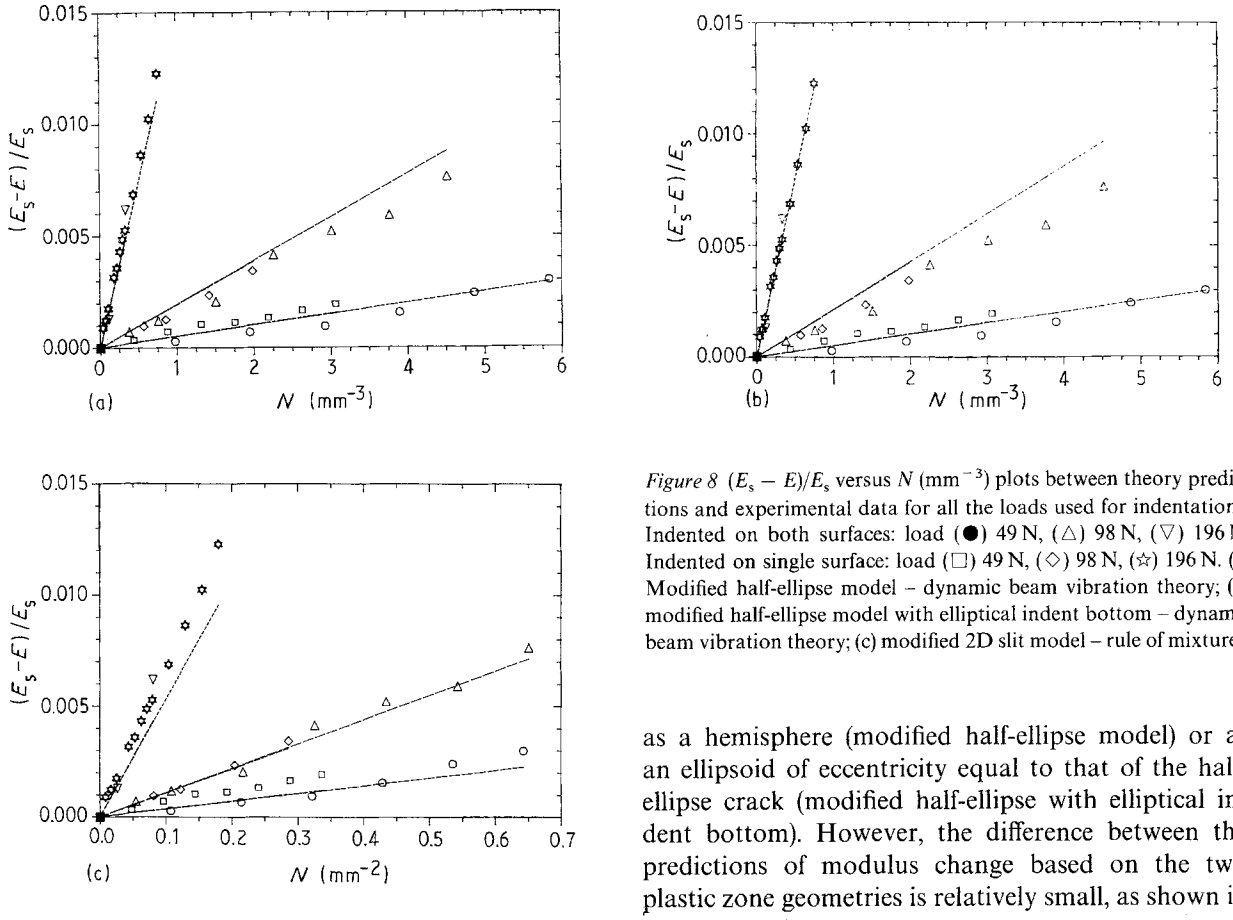

Figure 8 $(E_s - E)/E_s$ versus N (mm^{-3}) plots between theory predictions and experimental data for all the loads used for indentations. Indented on both surfaces: load (●) 49 N, (△) 98 N, (▽) 196 N. Indented on single surface: load (□) 49 N, (◇) 98 N, (☆) 196 N. (a) Modified half-ellipse model – dynamic beam vibration theory; (b) modified half-ellipse model with elliptical indent bottom – dynamic beam vibration theory; (c) modified 2D slit model – rule of mixtures.

changes were compared using a variety of model crack geometries (Figs 6–8 and Tables V–VIII).

Dynamic beam vibration theory predictions under the crack shape assumptions of modified half-ellipse cracks and modified half-ellipse cracks with elliptical indent bottom (three-dimensional models) (Table II in Part II [2]) best fit the experimental data for all the loads used in this study. This is encouraging since these models also best describe the observed geometry of the indentation crack, although no direct experimental observations were made to distinguish whether the plastically deformed zone itself was best described as a hemisphere (modified half-ellipse model) or as an ellipsoid of eccentricity equal to that of the half-ellipse crack (modified half-ellipse with elliptical indent bottom). However, the difference between the predictions of modulus change based on the two plastic zone geometries is relatively small, as shown in Fig. 8a and b.

Thus for realistic crack geometries, the surface-limited microcrack models developed here [1, 2] are in relatively good agreement with the experimentally observed trends of a linear increase in $(E_s - E)/E_s$ (the fractional or normalized modulus change) with increasing N, the crack number density. In addition, predicted values of the $(E_s - E)/E_s$ versus N slope from the data are in relatively good agreement with theoretical results for realistic geometries (corrected or modified to account for the plastic zone ligament for indentation cracks). The predictions of changes in $(E_s - E)/E_s$ versus N slope as a function of crack alignment [2] was not tested in this study.

Appendix: Porosity dependence of Young's modulus in unindented (polished) alumina specimens

The Young's moduli of unindented (polished) alumina specimens decreased as the porosity increased. In this study, the volume fraction porosity of the specimens ranged from about 0.060 to 0.075, based on a theoretical density of 3.98 g/cm^{-3} for alumina. In this appendix, we show that moduli measured for the undamaged alumina specimens are reasonable in terms of known modulus–porosity relations.

Two commonly used Young's modulus–porosity relations are [27]

$$E = E_0 e^{-kP} \quad \text{(A1)}$$

$$E = E_0 (1 - mP) \quad \text{(A2)}$$

where E = Young's modulus at porosity volume fraction P, E_0 = Young's modulus at zero porosity volume fraction ($P = 0$), P = volume fraction porosity and k, m = empirical constants. Phani [28] and Phani and Niyogi [29] suggested that the Young's modulus porosity relationship may be expressed as

$$E = E_0 (1 - P)^n \quad \text{(A3)}$$

where n is an empirical constant.

Bounds for E_0, the theoretically dense value for the Young's modulus of polycrystalline alumina, can be estimated from the single-crystal modulus data. The Voigt (upper bound) and Reuss (lower bound) values for polycrystalline alumina are 408.5 and 398.3 GPa, respectively [30]. In Equations A1–A3, E_0 was taken as 403.4 GPa, which is the arithmetic mean of the Voigt and Reuss bounds. Values of $k = 3.2$, $m = 2.9$ and $n = 3.1$ were determined via a least-squares fit of the modulus–porosity data to Equations A1, A2 and A3, respectively. Correlation coefficients of 0.935, 0.934 and 0.934 were obtained for the least-squares fit to Equations A1, A2 and A3, respectively.

References

1. E. D. CASE and Y. KIM, *J. Mater. Sci.* **28** (1993) 1885.
2. *Idem, ibid.* **28** (1993) 1901.
3. B. BUDIANSKY and R. J. O'CONNELL, *Int. J. Solids Struct.* **12** (1976) 81.
4. A. HOENIG, *ibid.* **15** (1979) 137.
5. N. LAWS and J. R. BROCKENBROUGH, *ibid.* **23** (1987) 1247.
6. H. P. KIRCHNER and E. D. ISSACSON, *J. Amer. Ceram. Soc.* **65** (1982) 55.
7. H. P. KIRCHNER, *ibid.* **67** (1984) 347.
8. B. L. SYMONDS, R. F. COOK and B. R. LAWN, *J. Mater. Sci.* **18** (1983) 1306.
9. A. G. EVANS and E. A. CHARLES, *J. Amer. Ceram. Soc.* **59** (1976) 371.
10. B. R. LAWN and D. B. MARSHALL, *ibid.* **62** (1979) 347.
11. G. R. ANSTIS, P. CHANTIKUL, B. R. LAWN and D. B. MARSHALL, *ibid.* **64** (1981) 533.
12. F. FORSTER, *Z. Metallkde* **29**(4) (1937) 109.
13. G. PICKETT, *ASTM Proc.* **45** (1945) 846.
14. D. P. H. HASSELMAN, "Tables for the Computation of Shear Modulus and Young's Modulus of Elasticity from Resonant Frequencies of Rectangular Prisms" (Carborundum Co., Niagara Falls, New York, 1961).
15. S. SPINNER and W.E. TEFFT, *ASTM Proc.* **61** (1961) 1221.
16. Y. KIM, W. J. LEE and E. D. CASE, "Reinforced Aluminosilicate Glass Ceramic Composite", in "Metal and Ceramic Matrix Composites: Processing, Modeling and Mechanical Behavior", Edited by R. B. Bhagat, A. H. Clauer, P. Kumar and A. M. Ritter (Minerals, Metals and Materials Society, Warrendale, PA, 1990) pp. 479–486.
17. *Idem*, in Proceedings of 5th Technical Conference, 1990, American Society for Composites (Technomic Press, Lancaster, PA, 1990) pp. 871–881.
18. Y. KIM and E. D. CASE, *J. Mater. Sci.* **27** (1992) 1537.
19. W. J. LEE and E. D. CASE, *Mater. Sci. Engng* **A119** (1989) 113.
20. *Idem, J. Mater. Sci.* **25** (1990) 5043.
21. P. F. BECHER, C. HSUEH, P. ANGELINI and T. N. TIEGS, *J. Amer. Ceram. Soc.* **71** (1988) 1050.
22. D. K. SHETTY, I. G. WRIGHT, P. N. MINCER and A. H. CLAUER, *J. Mater. Sci.* **20** (1985) 1873.
23. E. SCHREIBER, O. L. ANDERSON and N. SOGA, "Elastic Constants and Their Measurements" (McGraw-Hill, New York, 1974) Ch. 4.
24. D. B. MARSHALL and B. R. LAWN, *J. Amer. Ceram. Soc.* **63** (1980) 532.
25. E. R. FULLER, B. R. LAWN and R. F. COOK, *ibid.* **66** (1983) 314.
26. C. C. CHIU and E. D. CASE, *J. Mater. Sci.* **27** (1992) 2353.
27. J. C. WANG, *ibid.* **19** (1984) 809.
28. K. K. PHANI, *J. Mater. Sci. Lett.* **15** (1986) 747.
29. K. K. PHANI and S. K. NIYOGI, *ibid.* **5** (1986) 427.
30. G. SIMMONS and H. WANG, "Single Crystal Elastic Constants and Calculated Aggregate Properties: A Handbook", (MIT Press, Cambridge, Massachusetts, 1971) p. 329.

Received 27 April
and accepted 17 June 1992